


Label-free three-dimensional imaging and quantitative analysis of living fibroblasts and myofibroblasts by holotomographic microscopy

Francesca Sbrana¹ | Flaminia Chellini² | Alessia Tani² | Martina Parigi² |
Rachele Garella³ | Francesco Palmieri³ | Sandra Zecchi-Orlandini² |
Roberta Squecco³ | Chiara Sassoli² 

¹Biophysics Institute, National Research Council, Genoa, Italy

²Department of Experimental and Clinical Medicine, Section of Anatomy and Histology, Imaging Platform, University of Florence, Florence, Italy

³Department of Experimental and Clinical Medicine, Section of Physiological Sciences, University of Florence, Florence, Italy

Correspondence

Francesca Sbrana, Biophysics Institute,
National Research Council, Genoa, Italy.
Email: francesca.sbrana@ibf.cnr.it

Chiara Sassoli, Department of Experimental
and Clinical Medicine, Section of Anatomy and
Histology, Imaging Platform, University of
Florence, 50134 Florence, Italy.
Email: chiara.sassoli@unifi.it

Funding information

MUR (Ministry of University and Research,
Italy); Finanziamenti alla Ricerca di Ateneo;
University of Florence; European Commission;
NextGenerationEU; Missione 4 Componente
2; Dalla ricerca all'impresa; Innovation
Ecosystem RAISE "Robotics and AI for Socio-
economic Empowerment"; Grant/Award
Number: ECS00000035

Review Editor: Alberto Diaspro

Abstract

Holotomography (HT) is a cutting-edge fast live-cell quantitative label-free imaging technique. Based on the principle of quantitative phase imaging, it combines holography and tomography to record a three-dimensional map of the refractive index, used as intrinsic optical and quantitative imaging contrast parameter of biological samples, at a sub-micrometer spatial resolution. In this study HT has been employed for the first time to analyze the changes of fibroblasts differentiating towards myofibroblasts – recognized as the main cell player of fibrosis – when cultured in vitro with the pro-fibrotic factor, namely transforming growth factor- β 1. In parallel, F-actin, vinculin, α -smooth muscle actin, phospho-myosin light chain 2, type-1 collagen, peroxisome proliferator-activated receptor-gamma coactivator-1 α expression and mitochondria were evaluated by confocal laser scanning microscopy. Plasmamembrane passive properties and transient receptor potential canonical channels' currents were also recorded by whole-cell patch-clamp. The fluorescence images and electrophysiological results have been compared to the data obtained by HT and their congruence has been discussed. HT turned out to be a valid approach to morphologically distinguish fibroblasts from well differentiated myofibroblasts while obtaining objective measures concerning volume, surface area, projection area, surface index and dry mass (i.e., the mass of the non-aqueous content inside the cell including proteins and subcellular organelles) of the entire cell, nuclei and nucleoli with the major advantage to monitor outer and inner features in living cells in a non-invasive, rapid and label-free approach. HT might open up new research opportunities in the field of fibrotic diseases.

Research Highlights

- Holotomography (HT) is a label-free laser interferometric imaging technology exploiting the intrinsic optical property of cells namely refractive index (RI) to enable a direct imaging and analysis of whole cells or intracellular organelles.

- HT turned out a valid approach to distinguish morphological features of living unlabeled fibroblasts from differentiated myofibroblasts.
- HT provided quantitative information concerning volume, surface area, projection area, surface index and dry mass of the entire fibroblasts/myofibroblasts, nuclei and nucleoli.

KEYWORDS

fibrosis, holotomographic microscopy, label-free, myofibroblasts, quantitative phase imaging

1 | INTRODUCTION

Optical diffraction tomography (ODT), also known as holotomography (HT), is a cutting-edge label-free laser interferometric imaging technology. Analogous to X-ray computed tomography it combines holography and tomography techniques to analyze in three-dimensions (3D) different biological samples, including living individual cells, interacting cells and tissue slices (Hugonnet et al., 2021; Kim et al., 2014; Kim, Lee, Jung, et al., 2018; Park et al., 2018). Holography involves recording the interference pattern of light scattered off a sample, creating a hologram. Tomography, on the other hand, involves acquiring multiple holograms at multiple viewing angles to reconstruct a 3D representation of the object. HT exploits the intrinsic optical properties of biological samples namely refractive index (RI) to enable a direct imaging and analysis of whole cells or intracellular organelles without the need for a fixation step or the use of exogenous labeling agents or dyes. Indeed, RI value is used as an intrinsic optical and quantitative imaging contrast parameter linearly proportional to the concentration of biomolecules. Therefore, changes in the RI of a biological sample are directly related to sample density, thickness, morphology, cellular and subcellular structures' features (Kim & Guck, 2020). When light encounters such variations in RI it undergoes a phase delay. HT measures and quantifies both the amplitude and these phase shifts of the light, and computationally reconstructs a 3D map of RI values distribution (RI tomograms) within the sample faithfully recalling the cellular and subcellular structures' features. Since HT is able to reveal subtle changes in RI, at a sub-micrometer spatial resolution it can provide a wealth of details and thus high-resolution 3D images. Moreover, morphological and biochemical parameters of living unlabeled biological samples are quantitatively measured from the reconstructed 3D RI maps including, among others, the surface, projection area, volume, dry mass and lipid content (Kim, Lee, Shin, & Park, 2018; Park et al., 2018). Given its rapid, non-invasive and label-free approach without exhaustive sample preparation, HT has emerged as valid and powerful tool for biological sample imaging, in various research fields, such as cancer biology (Friedrich et al., 2020; Kim & Guck, 2020; Kim, Lee, et al., 2016; Salucci et al., 2020) hematology and immunology (Kang et al., 2022; Kim et al., 2014; Kim et al., 2019; Kim et al., 2022; Kim, Yoon, et al., 2016; Koo et al., 2019; Lee et al., 2020; Park et al., 2016; Yoon et al., 2017) neuroscience (Lee et al., 2023; Yang et al., 2017), microbiology and marine biology (Choi et al., 2021; Costa et al., 2023; Di Giannantonio et al., 2022; Jung et al., 2018; Oh et al., 2020).

Given that cellular and subcellular morpho-functional modifications occur during different cell processes such as growth, division, differentiation, neoplastic transformation or death, HT may represent a valid tool to monitor and study these biological events.

In this study, HT was applied for the first time to analyze living proliferating and differentiating NIH/3T3 fibroblasts, at a single cell level. In particular, the cells were cultured in standard growth condition and in differentiating condition in the presence of the transforming growth factor (TGF)- β 1 to induce fibroblast-to-myofibroblast (Myof) transition (Squecco et al., 2020). Myofs display features of both contractile smooth muscle cells and fibroblasts synthesizing components of extracellular matrix (ECM), hence the name (Pakshir et al., 2020). Among other progenitors, these cells come from the differentiation of fibroblasts resident in the ECM. Upon a tissue damage, an integrated action of different mechanical, chemical (including profibrotic factors, mainly TGF- β 1) and cellular stimuli from the surrounding damaged microenvironment promotes the activation of fibroblasts that differentiate into Myofs. Mature well-differentiated Myofs exhibit a robust expression of α -smooth muscle actin (α -sma) and other contractile proteins incorporated in extensively developed and well-assembled stress fibers that are able to generate contractile forces functional to wound contraction (Younesi et al., 2024). When compared to fibroblasts, Myofs are larger and secrete higher amounts of ECM components especially type-1 collagen (Col-I). Moreover, even if Myofs are not regarded as electrically excitable cells, they show distinctive biophysical properties and trans-membrane ion currents typical of smooth muscle cells (Chilton et al., 2005; Kaur et al., 2013; Sassoli, Garella, et al., 2022; Squecco et al., 2020).

2 | MATERIALS AND METHODS

2.1 | Cell culture and treatments

Murine NIH/3T3 fibroblasts purchased from American Type Culture Collection (ATCC, Manassas, VA, USA Cat# CRL-6361, RRID: CVCL_6662) were grown in proliferation medium (PM), consisting of Dulbecco's Modified Eagle's Medium (DMEM; Sigma, Milan, Italy) containing 4.5 g/L glucose supplemented with 10% fetal bovine serum (FBS) and 1% penicillin/streptomycin (Sigma), at 37°C in a humidified atmosphere of 5% CO₂. They were induced to differentiate into Myofs by shifting them in differentiation medium

(DM) consisting of DMEM supplemented with 2% FBS and 2 ng/mL TGF- β 1 (PeproTech, IncRocky Hill, NJ, USA) for 24, 48 and 72 h, as previously reported (Chellini, Tani, Vallone, Nosi, Pavan, Bambi, Zecchi-Orlandini, & Sassoli, 2018).

2.2 | Morphological analyses

2.2.1 | Holotomography (HT) imaging and quantitative cell analysis

NIH/3T3 cells were cultured on glass dish substrate (TomoDish, Tomocube, Daejeon, Republic of Korea) in the different experimental conditions (in PM or in DM for different times) and then observed and quantitatively evaluated *in vivo* without any staining or pretreatment by using a commercial optical diffraction tomography system (Tomocube HT-2H; Tomocube Inc., Daejeon, Republic of Korea). The optical system, based on Mach-Zehnder interferometry, is equipped with a coherent monochromatic laser source ($\lambda = 532$ nm, 0.05 mW). The laser beam is split into two beam paths: the first beam passes through the sample and the second one is used as a reference beam. A digital micromirror device (DMD) placed onto the sample plane of the sample beam, is used to digitally manage the illumination of the sample at various angles rapidly and with high precise control. A high numerical aperture water immersion objective lens (NA = 1.2, UPLSAPO 60XW; Olympus, Tokyo, Japan) is used to illuminate the sample and a second high NA objective lens (NA = 1.2, UPLSAPO 60XW; Olympus, Tokyo, Japan) is used to collect the diffracted light from the sample. The spatially modulated hologram obtained as results of the interference between the diffracted light from the sample and the reference beam is collected and recorded as an image by a CMOS image sensor (FL3-U3-13Y3MC, FLIR Systems) (Figure 1). The images were acquired by using an exposure shutter of 1 ms. The experiments were all performed in triplicate ($n = 40$ cells for each experimental point).

Multiple 2D holograms, containing both the amplitude and phase data, are rapidly acquired (0.4 s for frame) at various illumination angles: from 49 illumination conditions, a normal incidence, and 48 azimuthally symmetric directions with a polar angle (64.5°). 3D RI distribution tomogram of the live and unlabeled cells is calculated as a matrix of RI voxel data by inversely solving the Helmholtz equation with Rytov approximation of weak scattering (Devaney, 1981; Wolf, 1969).

TomoStudio™ software (Tomocube Inc., Daejeon, Korea) has been used to generate, visualize and quantitatively elaborate the voxel data representing them: in 2D maximum intensity projection maps of RI value (2D MIP-HT, shown in gray scale); Z slice sectioning images (cross section along z axes, shown in gray scale) and in 3D RI based rendering map (3D-RI HT). The selected bands of RI, represented in pseudocolor scale, highlight cell morphology and intracellular components that have distinct RI values. The theoretically calculated lateral and axial spatial resolutions of the optical imaging system were 110 and 360 nm, respectively. The resolution of the RI values was less than 0.001. More detailed information on the principle of holotomography can be found elsewhere (Kim et al., 2013).

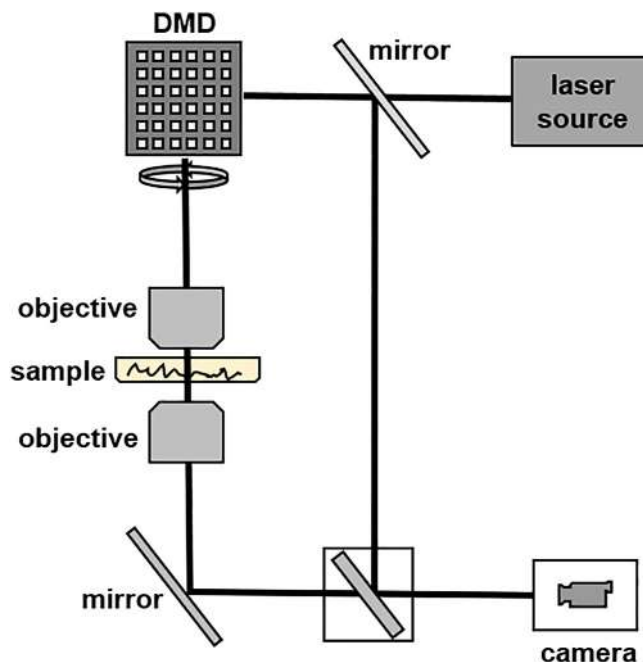


FIGURE 1 Schematic representation of the holotomography imaging system: Based on Mach-Zehnder interferometry, the laser beam is divided into two paths (sample and reference), that interfere with each other generating a hologram, collected by a camera. A digital micromirror device (DMD) manages the rotation of the illumination around the sample to generate a holotomogram.

For the morphological and biochemical analysis of NIH/3T3 cells, TomoAnalysis™ software (Tomocube Inc., Daejeon, Korea) was used. This software employs a deep-learning-based 3D U-Net architecture (Ryu et al., 2023) to automatically segment individual cells and subcellular organelles from holotomography data. The segmentation process differentiates cells and organelles, including the nucleus, nucleolus, plasma membrane, by generating identifying masks. Quantitative analysis was automated within the software, calculating cellular volume by voxel count and organelle-specific RIs, and surface area, projected area, through triangular meshing of segmented masks. The dry mass concentration (C) was determined using the following equation:

$$C = \frac{\frac{1}{N} \sum_i n_i - n_0}{RII}$$

where N is the number of segmented masks, n_i is the refractive index of each voxel, n_0 is the refractive index of the surrounding medium (1.3370), and the RII is set to 0.193 fL pg^{-1} for other organelles (Barer, 1953; Popescu et al., 2008; Zangle & Teitell, 2014; Zhao et al., 2011). The dry mass was calculated by summation of the dry mass values obtained at each voxel. The dry mass of each voxel was calculated by multiplying the dry mass concentration by the voxel volume. The sphericity index (ψ), a dimensionless parameter, quantifies the degree of cell roundness and is calculated by the ratio of the surface area of a sphere that has the same volume of the object of interest and the surface area of this object, according to $\psi = \pi^{1/3}(6V)^{2/3}/$

S, where V is the volume and S is the surface area. The sphericity index ranges value from zero for a laminar disc to unity for a sphere (Yang et al., 2017).

2.2.2 | Confocal laser scanning (CLS) microscopy

Indirect immunofluorescence analyses

Murine NIH/3T3 fibroblasts were grown on glass coverslips in PM or in DM for different times, fixed with 0.5% buffered Paraformaldehyde (PFA, Sigma) for 10 min at room temperature (RT) and processed as previously reported (Squecco et al., 2020). Primary antibodies (overnight at 4°C): mouse monoclonal anti-vinculin (7F9) (1:100; Santa Cruz Biotechnology, Santa Cruz, CA, Cat# sc-73,614, RRID: AB_1131294), mouse monoclonal anti- α -smooth muscle actin (sma) (1:100; Abcam, Cat# ab7817, RRID AB_262054), rabbit polyclonal anti-Phospho-Myosin Light Chain (p-MLC) 2 (Ser-19) (1:100; Cell Signaling Technology, Danvers, MA, USA, Cat# 3671, RRID AB_330248), rabbit polyclonal anti-type-1 collagen (Col-I, 1:500; Abcam, Cambridge, UK, Cat# ab 34,710, RRID AB_731684) and mouse monoclonal anti-peroxisome proliferator-activated receptor-gamma coactivator (PGC)-1 α (D-5) (1:100; Santa Cruz Biotechnology, Cat# sc-518,025, RRID AB_2890187). Secondary antibodies (1 h at RT): goat anti-mouse or anti-rabbit Alexa Fluor 488-conjugated IgG (1:200; Molecular Probes-Thermo Fisher Scientific, Eugene, OR, USA, anti-mouse: Cat# A11001, RRID AB_2534069, anti-rabbit: Cat# A11034, RRID AB_2576217) or goat anti-mouse or anti-rabbit Alexa Fluor 568-conjugated IgG (1:200; Molecular Probes-Thermo Fisher Scientific, Eugene, OR, USA, anti-mouse: Cat# A11004, RRID AB_2534072, anti-rabbit: Cat# A11036, RRID AB_10563566). Negative controls were carried on by replacing primary antibodies with non-immune serum and the cross-reactivity of the secondary antibodies was assessed by omitting the primary antibodies.

F-actin staining

To reveal F-actin filament assembly (stress fiber-like structures), fixed cells were permeabilized with cold acetone for 3 min and incubated before with a blocking solution (1% bovine serum albumin (BSA; Sigma)) for 40 min and then with Alexa Fluor 488-labeled phalloidin (1:40; Molecular Probes, Cat# A12379) for 20 min at RT.

Mitochondria staining

Living NIH/3T3 fibroblasts in the different experimental conditions were incubated with MitoTracker Red CMXRos (100 nM; Molecular Probes, Cat# M7512) before being fixed and processed for confocal immunofluorescence analysis of PGC-1 α .

Nuclei were counterstained with propidium iodide (PI, 1:100 for 30 s at RT; Molecular Probes, Cat# P3566) and the glass coverslips with the immunolabeled cells were mounted with an antifade mounting medium (Biomeda Gel mount; Electron Microscopy Sciences, Foster City, CA, USA), or with 4',6-diamidino-2-phenylindole (DAPI) contained in the Fluoroshield mounting medium (Sigma, Cat# F6057). Observations were performed under a Leica Stellaris 5 confocal microscope equipped with a white light source for fluorescence

measurements by using a Leica Plan Apo 63 \times /1.43NA oil immersion objective. Series of optical sections (1024 \times 1024 pixels each; pixel size 204.3 nm) 0.4 μ m in thickness were taken through the depth of the cells at intervals of 0.4 μ m and projected onto a single 'extended focus' image. Densitometric analyses of the mean fluorescence intensity of the different markers were performed on digitized images by using ImageJ 1.49v software (<https://imagej.nih.gov/ij/>) in 10 regions of interest (ROI; 100 μ m²) selected in 5 cells for each confocal stack (10 for each of the four experimental points performed in duplicate). The experiments were performed in triplicate (*n* for each experimental point = ROI = 100; number of examined cells for each experimental point = 50).

2.3 | Electrophysiological analyses

Electrophysiological records were performed by using the whole-cell patch clamp technique essentially as reported previously (Sassoli et al., 2016). The coverslip with the adherent cells was located in the proper chamber on the stage of the Nikon Eclipse TE200 inverted microscope (Nikon Europe BV, 1076 ER Amsterdam, The Netherlands) (Mannelli et al., 2022). Cells were bathed in physiological bath solution (mM): 150 NaCl, 5 KCl, 2.5 CaCl₂, 1 MgCl₂, 10 D-glucose and 10 HEPES (pH = 7.4 with NaOH). Patch pipettes were prepared from capillaries of borosilicate glass (GC150-7.5, Harvard apparatus LTD) using a vertical puller (Narishige, Tokyo, Japan) and were filled with the internal filling solution (mM): 130 KCl, 10 NaH₂PO₄, 0.2 CaCl₂, 1 EGTA, 5 MgATP and 10 HEPES (pH = 7.2). The patch pipette was put in a CV203BU head-stage (Axon Instruments, Foster City, CA) connected to a micro-manipulator (Narishige, Tokyo, Japan) and to an Axopatch 200 B amplifier (Axon Instruments, Foster City, CA) as reported in previous papers (Squecco et al., 2016). The patch pipettes tip resistance was around 1.5–2 M Ω when filled with the internal solution. Voltage-clamp protocol generation, on-line currents monitoring and data acquisition were achieved by the A/D-D/A interfaces (Digidata 1200; Axon Instruments) and Pclamp 6 software (Axon Instruments Foster City, CA). The resting membrane potential (RMP) was recorded in current clamp mode using a current stimulus $I = 0$ nA. To analyze the NIH/3T3 membrane passive properties, we switched to the voltage clamp mode of our device: we applied a negative step voltage pulse to -80 mV and a positive pulse to -60 mV, starting from a holding potential (HP) of -70 mV. In this way, we only elicited the passive currents, namely an early capacitive transient followed by a transmembrane leak current, I_m (Martella et al., 2021). The membrane linear capacitance, C_m , calculated by the capacitive transient, can be assumed as an index of the cell surface, since the membrane-specific capacitance is a constant value (about 1 μ F cm⁻²). Transmembrane currents flowing through mechanically activated channels were evoked by a voltage ramp protocol applied from 0 mV ranging from -120 to $+50$ mV in 500 ms. (Combe et al., 2023; Sassoli et al., 2016). In particular, to determine the current flowing through transient receptor potential canonical (TRPC) channels we made a point-by-point subtraction of the leak I_m recorded after the adding of the selective TRPC blocker gadolinium chloride (GdCl₃, 50 μ M;

Sigma–Aldrich) from the I_m elicited at the beginning of the experiment. To allow an appropriate comparison between cells of different size, the current values measured at each membrane potential from each cell were divided by their related C_m and plotted as current densities (I/C_m). Electrophysiological records were conducted at room temperature (22°C).

2.4 | Statistical analysis

Statistical analyses of 3D RI HT maps and CLS fluorescent signals were performed by using one-way ANalysis Of VAriance (ANOVA) with post-hoc Tukey HSD test calculator for comparing multiple treatments (https://astatsa.com/OneWay_Anova_with_TukeyHSD/). For the electrophysiological experiments, mathematical data processing and statistical analysis were performed off-line by Clampfit 9 (Axon Instruments) and Excel (Microsoft Office 2016, Microsoft corporation, Redmond, WA, USA). The normal distribution of data values was assessed by the Shapiro–Wilk test (<https://www.statskingdom.com/shapiro-wilk-test-calculator.html>). Statistical analysis of electrophysiological data was achieved by one-way ANOVA with Bonferroni's correction for multiple comparison.

The results of the experiments are reported as mean \pm standard deviation (SD) or mean \pm standard error (SE) of at least three independent experiments performed in triplicate and $p < .05$ has been

considered statistically significant. n indicates the number of cells investigated.

3 | RESULTS

3.1 | HT imaging, CLS microscopy analyses and electrophysiological recordings of fibroblasts and Myofs

3.1.1 | HT imaging

Live NIH/3T3 cells grown in PM or in DM to promote fibroblast-to-Myof transition, were analyzed by HT. 2D MIP-HT maps, z slice sectioning images and 3D-RI HT maps are reported in Figures 2, 3 and 4, respectively. These images enabled the observation of the morphology of a whole cell, of its boundaries and intracellular components and structures including, among the others, cytoplasm, nucleus and nucleoli. NIH/3T3 cells grown in PM (Figure 2a) showed the typical fusiform shape of fibroblasts with a centrally placed nucleus with circle or oval-like shaped boundaries and containing more nucleoli. In these cells the cytoplasm content appeared uniformly distributed throughout the cell. On the other hand, a growing broad polygonal shape increasing over differentiation time was well appreciated for NIH/3T3 cells cultured in DM for different times (Figure 2b–d).

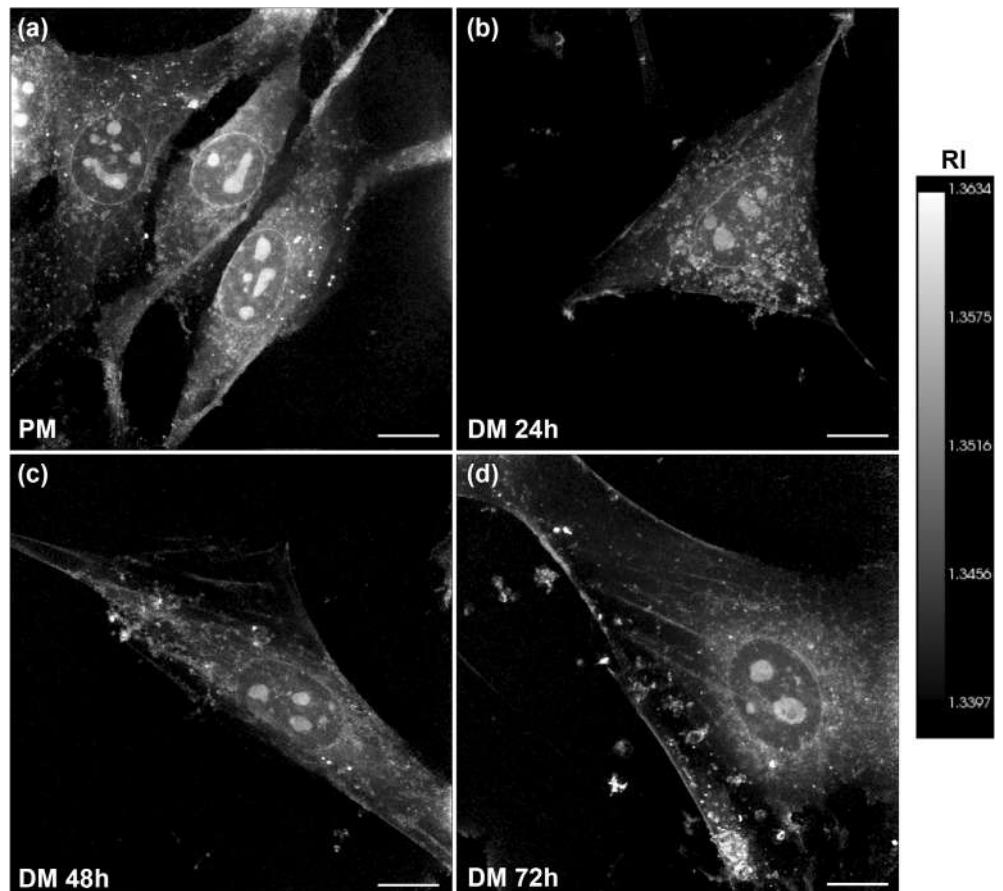


FIGURE 2 Representative 2D MPI-HT maps of NIH/3T3 cells cultured in (a) proliferation medium (PM: DMEM + 10% FBS) for 24 h or in (b–d) differentiation medium (DM: DMEM + 2% FBS + 2 ng/mL TGF- β 1) for the indicated times to promote fibroblast-to-Myof transition. Scale bar: 10 μ m. The gray scale indicates the refractive index (RI) range values.

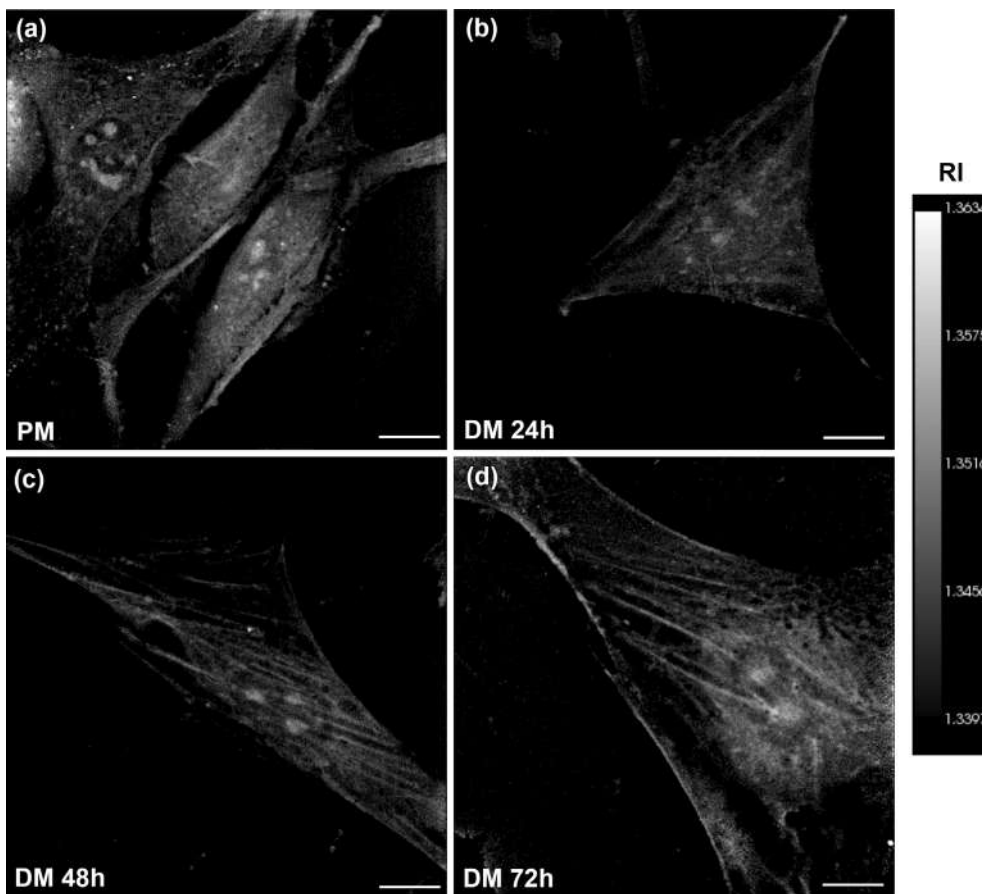


FIGURE 3 Representative Z slice sectioning images of NIH/3T3 cells cultured in (a) proliferation medium (PM: DMEM + 10% FBS) and in differentiation medium (DM: DMEM FBS 2% + 2 ng/mL TGF- β 1) for (b) 24 h, (c) 48 h and (d) 72 h. Scale bar: 10 μ m. The gray scale on the right indicates the refractive index (RI) range values.

Moreover, differentiating cells exhibited a slightly more elongated nucleus with fewer nucleoli as compared to proliferating cells (mean value of number of nucleoli: PM, 6.8 ± 0.1 ; DM 24 h, 4.2 ± 0.2 ; DM 48 h, 4.4 ± 0.2 ; DM 72 h, 3.7 ± 0.1 ; p vs. PM <0.01). They also displayed a different arrangement of the cytoplasm components that appeared more aggregated in the perinuclear region, especially in the cells cultured in DM for 72 h (Figure 2d). Of note, at the periphery of cells cultured for 48 and 72 h in DM, filamentous structures running through the cytoplasm and reaching the nucleus were also observable as well as plaques placed in the membrane periphery. After 72 h of culture in DM these filaments were more marked and bundled reaching the nucleus.

Such filamentous structures were best appreciable in the Z slice sectioning images reported in Figure 3 and in the Videos S1–S4. Moreover, moving along the z-axis of the sectioning, a highly elaborated network of membranous structures surrounding the nucleus can be also well distinguished.

The 3D HT maps, created as 3D RI-based rendering images and the relative cross section XY, YZ and XZ highlighted the features of the intracellular structures (Figure 4 and Videos S5–S8). The different pseudo-coloring represents different bands of RI values linked to: plasmamembrane in black color ($1.3405 \leq \text{RI} \leq 1.3412$); cytoplasm in brown color ($1.3421 \leq \text{RI} \leq 1.3426$); perinuclear cytoplasm in green ($1.3488 \leq \text{RI} \leq 1.3503$) and nucleolus in blue color ($1.3526 \leq \text{RI} \leq 1.3594$). Cytoplasm exhibits a lower RI value than the perinuclear

cytoplasm; the nucleolus, identified as the clusters inside the nucleus, clearly visualized through its boundaries in green, exhibited the highest RI values according to previous literature (Kim & Guck, 2020).

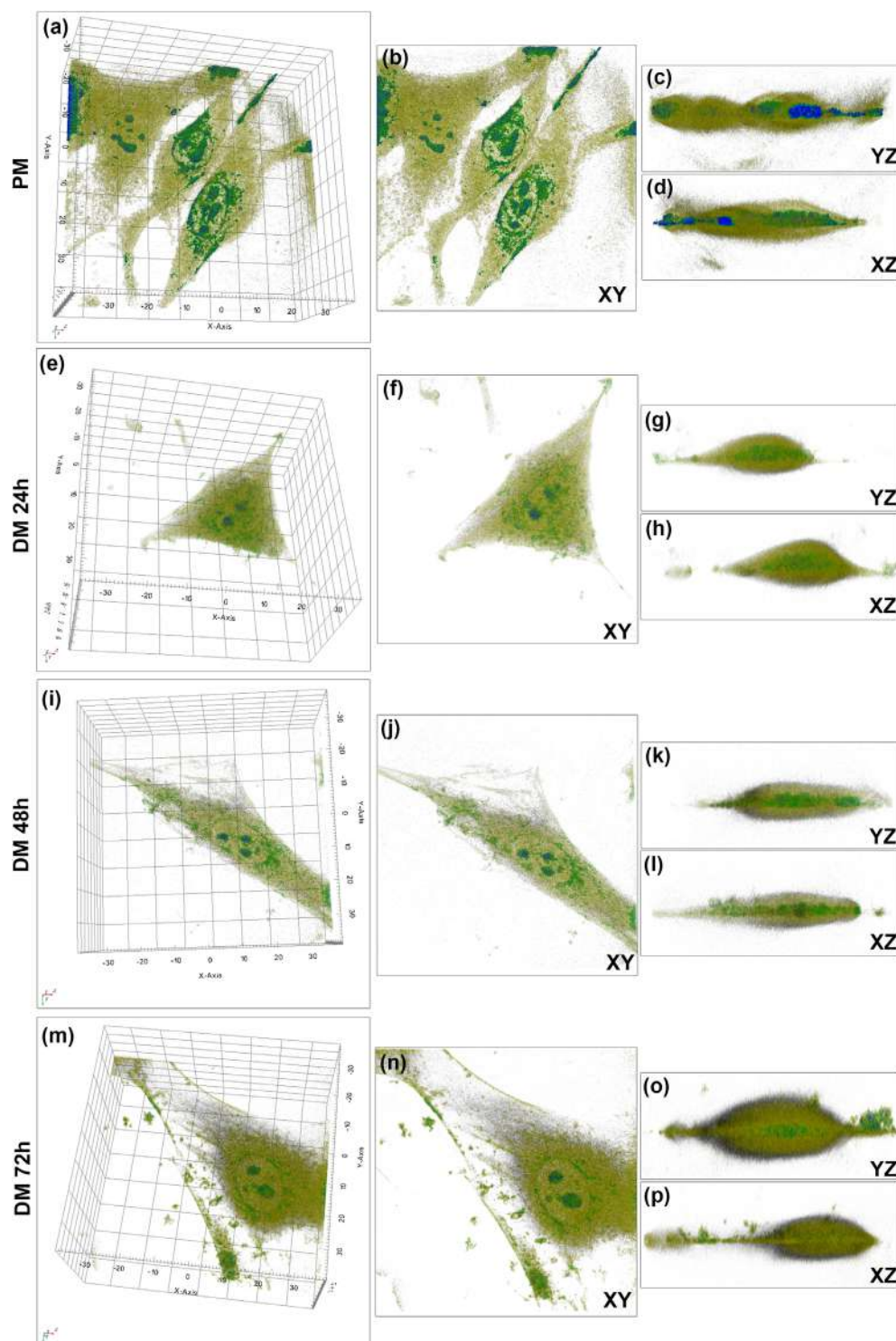
3.1.2 | CLS microscopy analysis

CLS microscopy analysis was performed to assess the assembly of distinctive structures and organelles and the expression of the main recognized markers of Myofs. In particular, first it was performed on cells cultured in the different experimental conditions and fixed to evaluate F-actin organization by labeling the cells with Alexa-488 conjugated phalloidin. Moreover, the expression and localization of the focal adhesion protein vinculin, α -sma (the most reliable marker of Myofs), p-MLC2 (the activated form of MLC2 correlated with myosin ATPase activity and muscle contraction) were evaluated by means indirect immunofluorescence techniques.

Fibroblasts cultured in PM did not exhibit robust cytoskeletal F-actin filaments (Figure 5a,i,m,q). These cells expressed low levels of vinculin (Figure 5e,i,m,r) as well as of α -sma (Figure 6a,i,m,q) and of p-MLC2 (Figure 6e,i,m,r) that appeared with a dot-like staining and mainly dispersed throughout the cytoplasm.

By contrast, when cultured in DM for 24 h the cells showed changes in their shape becoming more polygonal. In addition, they started to display thin F-actin positive stress fiber-like structures

FIGURE 4 Representative 3D HT maps (a, e, i, m; scale in μm) and XY (b, f, j, n), YZ (c, g, k, o) and XZ (d, h, l, p) projections of NIH/3T3 cells cultured in (a–d) proliferation medium (PM: DMEM + FBS 10%) and in differentiation medium (DM: DMEM + FBS 2% + 2 ng/mL TGF- β 1) for (e–h) 24 h, (i–l) 48 h and (m–p) 72 h. Black color $1.3405 \leq \text{RI} \leq 1.312$ plasma membrane; brown color $1.3421 \leq \text{RI} \leq 1.3426$ cytoplasm; green color $1.3488 \leq \text{RI} \leq -1.3503$ perinuclear cytoplasm; blue color $1.3526 \leq \text{RI} \leq -1.3594$ nucleolus.



typical of proto-Myofs (Tomasek et al., 2002) (Figure 5b,j,n,q) concomitantly to an increase of vinculin (Figure 5f,j,n,r) and α -sma (Figure 6b,j,n,q) expression. In these cells undergoing differentiation, although the expression levels of p-MLC2 appeared comparable to those of cells cultured in PM, such a protein was detected into filamentous structures (Figure 6f,j,n,r). After 48 h of culture in DM and, even more after 72 h, as expected, the cells exhibited all the typical features of well differentiated Myofs. Indeed they appeared larger, with a more polygonal shape, a prominent F-actin stress fiber network

across cytoplasm (Figure 5c,d,k,l,o,p,q) and a strong immunoreactivity for vinculin mainly clustered in plaques attached at the ends of the actin filamentous structures (Figure 5g,h,k,l,o,p,r). Concomitantly, these cells exhibited a robust expression of α -sma (Figure 6c,d,k,l,o,p,q) and of p-MLC2 (Figure 6g,h,k,l,o,p,r) incorporated into the stress fibers. In addition, CLS microscopy analysis of mitochondria by means the staining with mitotracker and immunostaining with antibodies against PGC-1 α , a crucial regulator of mitochondrial biogenesis, unraveled an increase of the fluorescence signals intensity related to both

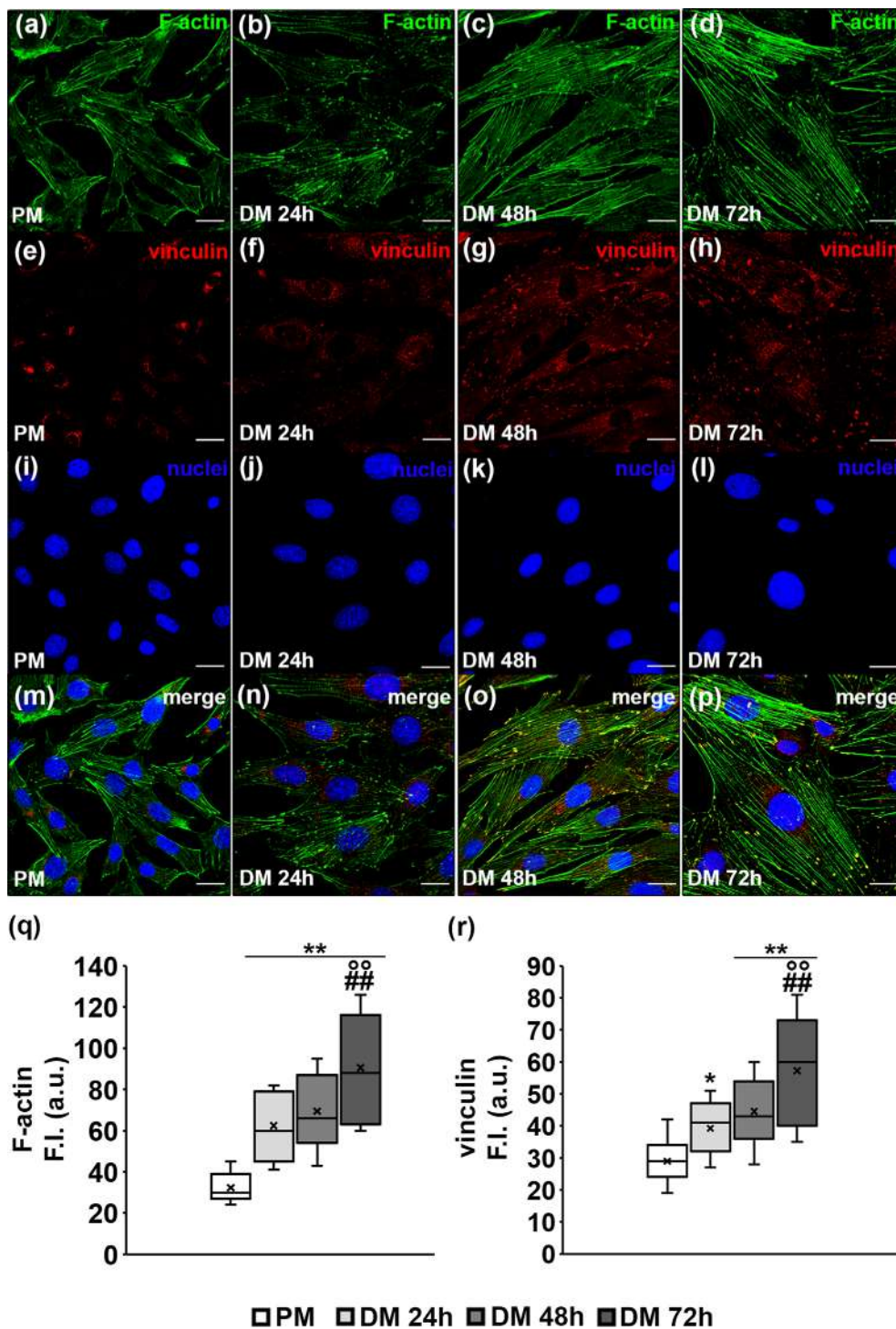


FIGURE 5 CLS microscopy analyses of F-actin filaments and vinculin expression. NIH/3T3 cells were grown on glass coverslips in proliferation medium (PM: DMEM + 10% FBS) for 24 h or in differentiation medium (DM: DMEM + 2% FBS + 2 ng/mL TGF- β 1) for different times (24, 48 and 72 h) to promote fibroblast-to-Myof transition. Representative images of fixed cells (a–d) stained with Alexa 488-conjugated phalloidin to reveal F-actin filaments (green) and (e–h) immunostained for vinculin expression (red). (i–l) Nuclei are counterstained with DAPI (blue). (m–p) Merged images. Scale bar: 20 μ m. (q, r) Densitometric analyses of the fluorescence intensity (F.I.) in arbitrary units (a.u.) of F-actin and vinculin respectively performed as indicated in Materials and Methods. Data are the mean \pm SD. One-way ANOVA with Tukey's post hoc test. Significance of differences: * $p < .05$, ** $p < .01$ versus PM; $^{\circ\circ} p < .01$ versus DM 24 h; ## $p < .01$ versus DM 48 h.

markers in the more differentiated cells (Figure 7a–n). These results suggested the occurrence of mitochondrial biogenesis during fibroblast-to-Myof transition, useful to sustain the energy demand required for cell differentiation and Myof functionality according with previous literature (Negmadjanov et al., 2015). Furthermore, the immunocytochemical analysis for Col-I expression displayed a robust increase of such protein in cells cultured in DM, especially for 72 h, as compared to cells cultured in PM (Figure 7o–s). The cytoplasmic Col-I staining appeared with a peculiar pattern of distribution consistent with the protein localization in the cisternae of the endoplasmic

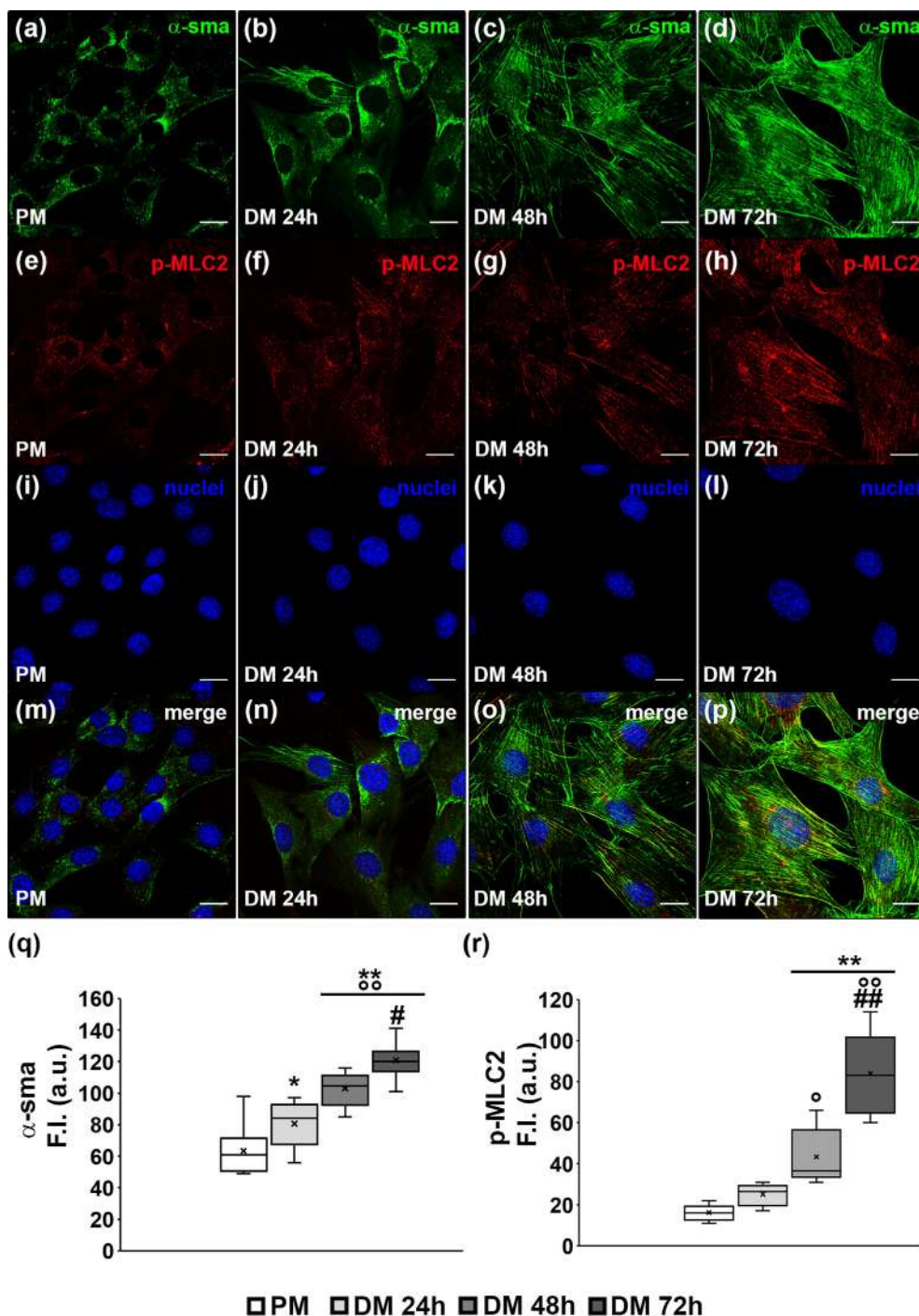
reticulum and Golgi vesicles, as expected for a mature Myof in an active phase for ECM components' synthesis. This represents a distinctive feature, likely discriminating fibroblasts from Myofs.

3.1.3 | Electrophysiological recordings

The morphological observations enabling to distinguish fibroblasts from differentiated Myofs were strongly supported by the electrophysiological functional analysis of the plasmamembrane passive

FIGURE 6 CLS

immunofluorescence analyses of α -smooth muscle actin (sma) and phospho-myosin light chain (p-MLC) 2 expression and organization. NIH/3T3 cells were grown on glass coverslips in proliferation medium (PM: DMEM + 10% FBS) for 24 h or in differentiation medium (DM: DMEM + 2% FBS + 2 ng/mL TGF- β 1) for different times (24, 48 and 72 h). Representative immunofluorescence images of fixed cells immunostained for (a–d) α -smooth muscle actin (sma) (green) and (e–h) phospho-Myosin Light Chain 2 (p-MLC2, red) expression. (i–l) Nuclei are counterstained with DAPI (blue). (m–p) Merged images. Scale bar: 20 μ m. (q, r) Densitometric analyses of the fluorescence intensity (F.I.) in arbitrary units (a.u.) of α -sma (q) and p-MLC2 (r) performed as indicated in Materials and Methods. Data are the mean \pm SD. One-way ANOVA with Tukey's post hoc test. Significance of differences: * p < .05, ** p < .01 versus PM; $^{\circ}$ p < .05, $^{\circ\circ}$ p < .01 versus DM 24 h; # p < .05, ## p < .01 versus DM 48 h.



properties. The analysis of RMP, which uses to be more depolarized when fibroblasts acquire a more differentiated myofibroblastic phenotype, showed indeed more positive values when cells were grown in DM compared to those in PM, at any time point tested (Table 1; Figure 8a–c). This observed membrane depolarization in cells cultured in DM is well related to the acquisition of a more activated phenotype, more prone to contractile activity, and therefore to a more differentiated Myof. The evaluation of C_m (Table 1, Figure 8a,b,d), elicited by the pulse protocol depicted in Figure 8d (inset), showed significantly higher values for cells in DM compared to those in PM, at

any time point tested. Since C_m represents an index of cell surface, this recorded increase is well related to the achievement of a more extended cell surface as expected when the typically fusiform fibroblasts become larger and more polygonal Myofs, and as actually observed by the morphological analyses.

To analyze in depth the functional features of cells undergoing differentiation we also investigated the possible activation of Transient Receptor Potential Canonical 1 (TRPC1) channel which is expected to improve, on the basis of previous investigations (Sassoli et al., 2016). To this aim, we evoked the transmembrane currents by

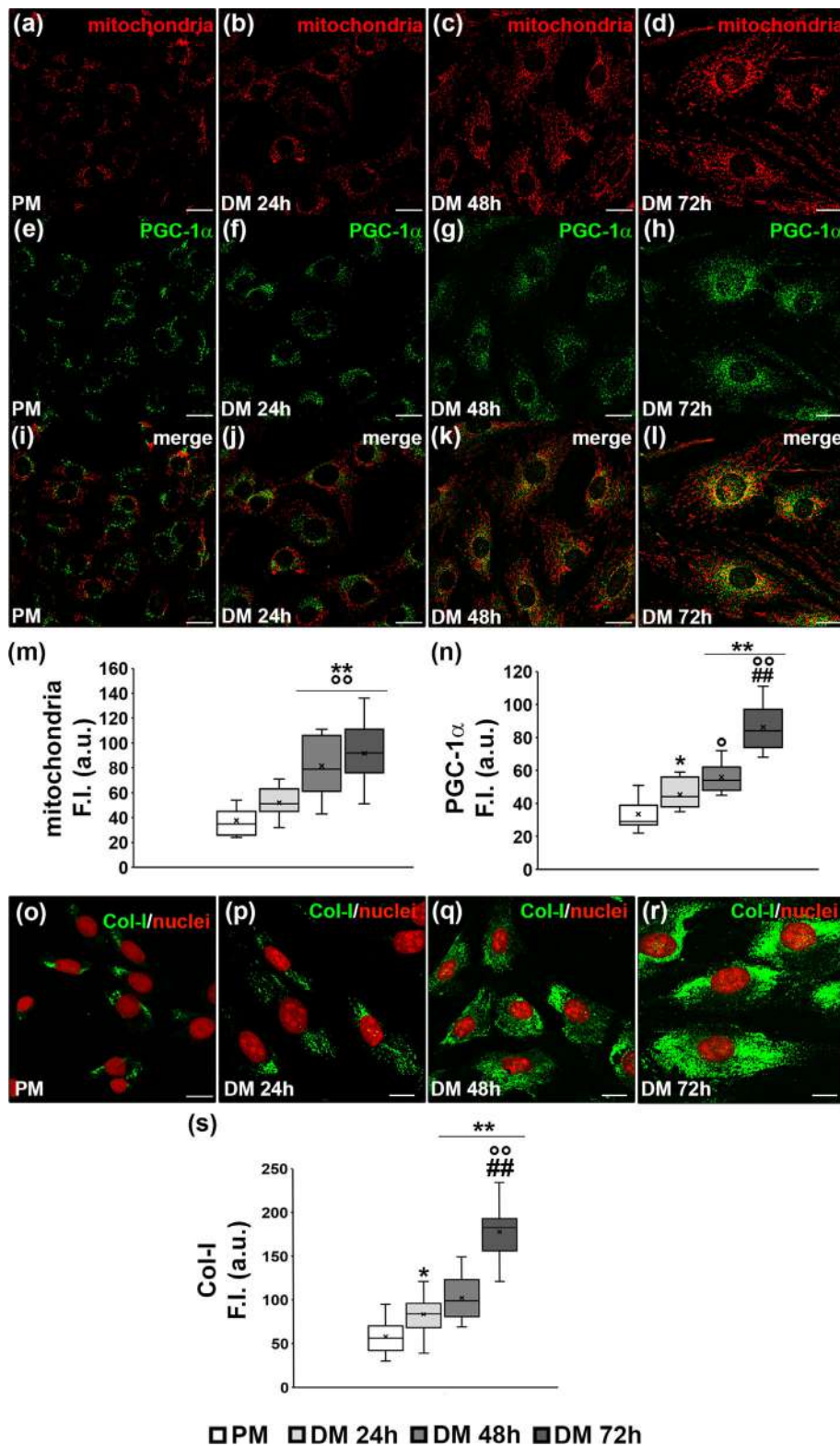


FIGURE 7 CLS microscopy analyses of mitochondria, peroxisome proliferator-activated receptor-gamma coactivator (PGC)-1 α and type-1 collagen (Col-I) expression. NIH/3T3 cells were cultured on glass coverslips in proliferation medium (PM: DMEM + 10% FBS) for 24 h or in the differentiation medium (DM: DMEM + 2% FBS + 2 ng/mL TGF- β 1) for different times (24, 48 and 72 h). Representative fluorescence images of cells (a–d) labeled with mitotracker to mark mitochondria (red), and immunostained for (e–h) PGC-1 α and (o–r) Col-I expression (green). (i–l) Merged images. (o–r) Nuclei are counterstained with propidium iodide (PI) (red). Scale bar: 20 μ m. (m, n, s) Densitometric analyses of the fluorescence intensity (F.I.) in arbitrary units (a.u.) of mitochondria, PGC-1 α and Col-I respectively performed as indicated in Materials and Methods. Data are the mean \pm SD. One-way ANOVA with Tukey's post hoc test. Significance of differences: * p < .05, ** p < .01 versus PM; \circ p < .05, $\circ\circ$ p < .01 versus DM 24 h; ## p < .01 versus DM 48 h.

the voltage ramp protocol of stimulation (Figure 8e) in the cells cultured in PM and in DM for 72 h. We isolated TRPC1 currents by the mathematical procedure described in Methods. As shown by a representative example reported in Figure 8g, the Gd³⁺-sensitive TRPC1 current amplitude normalized for C_m was bigger in cells cultured in

DM (slope = 0.13) than in PM (slope = 0.08) (Figure 8f) strongly suggesting a more pronounced TRPC1 activation in differentiated Myof. This allows a greater Ca²⁺ influx that, in turn, can contribute to membrane depolarization and can support cell contraction typical of a Myof.

TABLE 1 Plasmamembrane passive properties.

	PM	DM 24 h	DM 48 h	DM 72 h
RMP (mV)	-52.2 ± 11.7 $n = 15$	$-42.4 \pm 6.7^*$ $n = 14$	$-41.7 \pm 2.6^{**}$ $n = 7$	$-35.3 \pm 8.5^*$ $n = 5$
Cm (pF)	11.5 ± 5.0 $n = 8$	$20.5 \pm 5.3^*$ $n = 4$	$22.3 \pm 4.6^{**}$ $n = 6$	$28.0 \pm 11.8^{**}$ $n = 7$

Note: NIH/3T3 cells were cultured in the proliferation medium (PM: DMEM + 10% FBS) for 24 h or in the differentiation medium (DM: DMEM + 2% FBS + 2 ng/mL TGF- β 1) for the indicated times. Data are expressed as mean \pm SD. n = number of investigated cells, * p < .05, ** p < .01 versus PM (One way ANOVA, Bonferroni post hoc test).

Abbreviations: Cm, membrane capacitance; RMP, resting membrane potential.

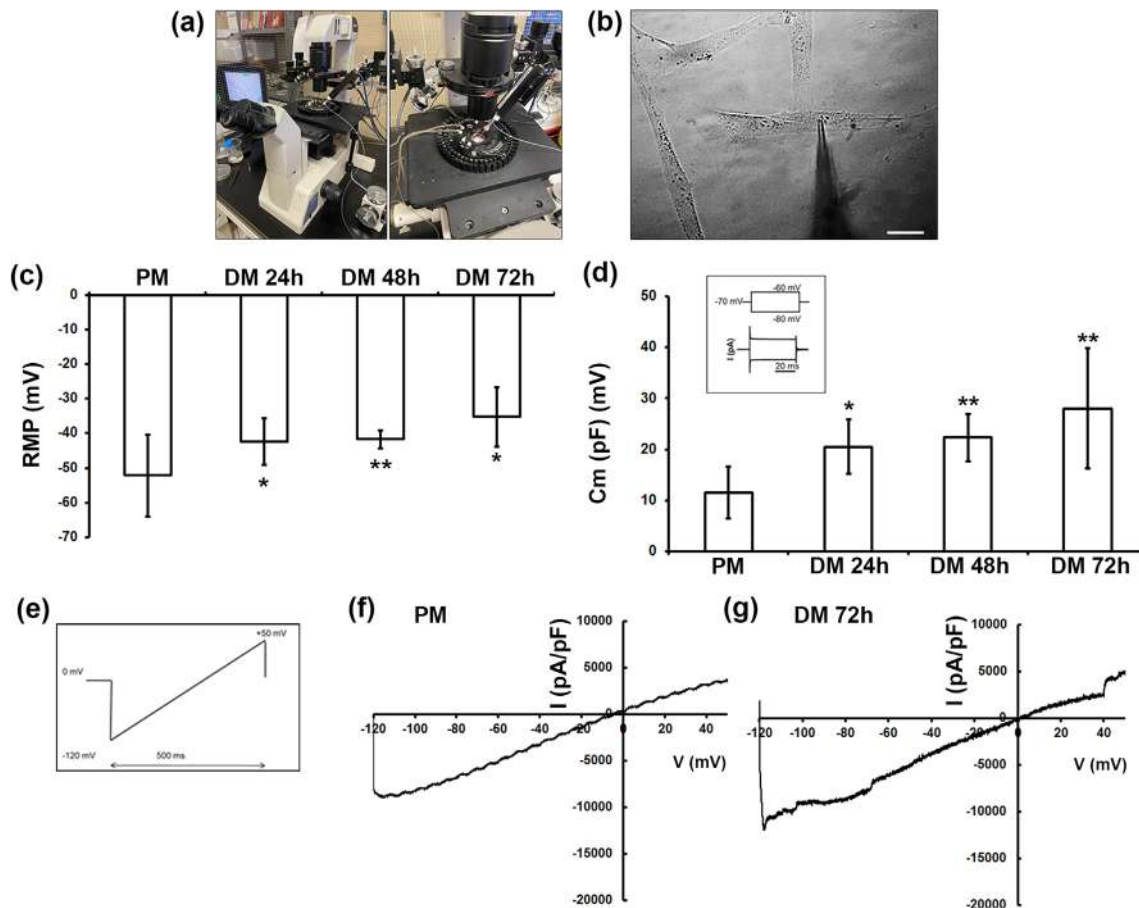


FIGURE 8 Electrophysiological recordings. (a) Experimental set up for whole cell patch analysis records Nikon Eclipse TE200 inverted microscope (detail). (b) Representative cell impaled by the patch pipette. Scale bar: 20 μ m. (c) Resting membrane potential (RMP, in mV) measured in current clamp from cells in proliferation medium (PM: DMEM + 10% FBS) for 24 h or in the differentiation medium (DM: DMEM + 2% FBS + 2 ng/mL TGF- β 1) for different times (24, 48 and 72 h). (d) Analysis of membrane capacitance (Cm) from cells in PM, DM 24 h, DM 48 h and DM 72 h (pulse protocol and representative current response in the inset). (e) Voltage ramp protocol applied from HP = 0 mV ranging from -120 to +50 mV in 500 ms. (f, g) Representative Gd³⁺-sensitive transient receptor potential canonical channel (TRPC) 1 currents obtained by the ramp protocol application. The normalized current amplitude is consistently bigger from cells cultured in DM 72 h (g) compared to that in PM (f). Data are expressed as mean \pm SD. n = number of investigated cells, * p < .05, ** p < .01 versus PM (One way ANOVA, Bonferroni post hoc test).

3.2 | Quantification of morphological and biochemical parameters using RI maps

A quantitative analysis was performed on 3D RI HT maps for NIH/3T3 cells cultured in all experimental conditions (PM and in DM 24, 48 and 72 h). Morphological (volume, surface area, projection area, sphericity index) and biochemical (dry mass) parameters were

extracted from the segmentation process of the map (Figure 9a) evaluated for the individual whole cells (Figure 9b) and nucleus (Figure 9c) on the basis of RI values. Likewise, volume and dry mass were evaluated for nucleolus (Figure 9d). Of note, the mean values of volume, surface area and projection area of the whole cell in DM conditions significantly increased with respect to PM condition; such values increased also with the differentiation time, in perfect agreement with

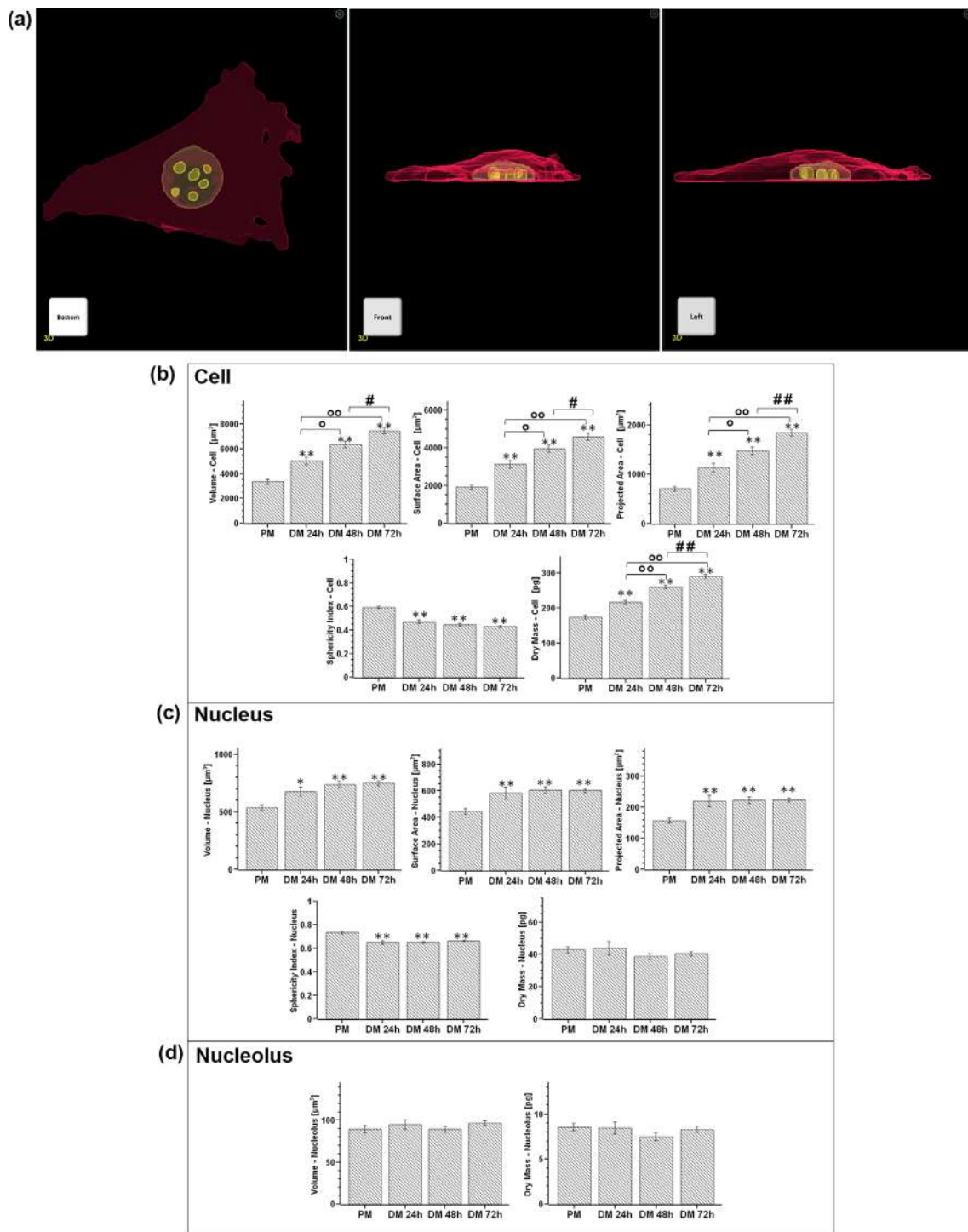


FIGURE 9 Quantitative analysis on 3D RI HT maps. (a) Plane projection of segmented mask of the cell (in DM) as visual output derived from the segmentation process. (b, c) Quantitative analyses of volume, surface area, projected area, sphericity index and dry mass for whole NIH/3T3 cells and their nuclei in proliferation medium (PM: DMEM + 10% FBS) and in differentiation medium (DM: DMEM + 2% FBS + 2 ng/mL TGF- β 1) for 24, 48 and 72 h. (d) Quantitative analysis of volume and dry mass of nucleoli of the cells in the indicated experimental conditions. Data are expressed as mean \pm SE value; * p < .05, ** p < .01 versus PM; ° p < .05, °° p < .01 versus DM 24 h; # p < .05 versus DM 48 h (One-way ANOVA with Tukey's post hoc test).

the observed morpho-functional changes occurring during the acquisition of a Myof phenotype (Figure 9b) coming from both HT and CLS imaging and electrophysiological recordings.

The mean value of the sphericity index of the whole cell slightly decreased in DM condition with respect to PM condition (0.59 ± 0.01 in PM and 0.46 ± 0.01 , 0.44 ± 0.01 , 0.42 ± 0.01 in DM). These mean

values did not significantly change over differentiation time (Figure 9b). The mean dry mass values of the whole cell over the differentiation time significantly increased with respect to the PM condition, reaching the maximum values after 72 h of culture (Figure 9b).

Moreover, volume, surface area, projection area, sphericity and dry mass of nuclei were extracted for each single cell. The mean values of these parameters are reported in the graphs in Figure 9c. The mean values of nuclear volume, surface area and projection area significantly increased from PM to DM conditions and did not change over differentiation time. The mean value of sphericity index slightly but significantly decreased in DM as compared to PM, and did not change over differentiation time. The mean value of the dry mass of the nuclei remains unchanged from PM to DM condition. Finally, the mean values of volume of nucleolus and of their dry mass did not show statistically significant differences among the different experimental conditions (Figure 9d).

4 | DISCUSSION

The present work is, to the best of our knowledge, the first application of HT to analyze the changes of fibroblasts differentiating towards a myofibroblastic phenotype when cultured *in vitro* in the presence of the well-known profibrotic agent TGF- β 1. We revealed a high congruence between the results of HT imaging and quantitative analyses and those obtained by CLS microscopy that, in addition, aligned with the plasmamembrane electrophysiological functional features.

Fibroblast-to-Myof differentiation process is regarded as fundamental during both physiological and pathological aberrant response to a tissue injury (Weiskirchen et al., 2019). In the case of tissue lesion Myofs are recognized as the cells primarily responsible for producing and depositing high amounts of ECM components. These form a transient scar enabling wound size reduction and closure. Although imperfect, this repair guarantees a rapid restoration of tissue integrity and function at best. The physiological repair process proceeds with the provisional scar degradation concomitantly to Myofs' disappearance via apoptosis and/or senescence or the possible return to a quiescent state. Conversely, in the case of a chronic or extended damage or in the presence of a persevering inflammatory stimulus, Myofs persist and remain in an activated functional state. This causes a maladaptive reparative response with tissue fibrotic scarring that irreversibly replaces the normal tissue structure and that eventually may lead to organ impairment. Moreover, Myofs have been described in many multifactorial disorders where fibrosis plays a main role (Sassoli, 2022; Younesi et al., 2024; Zeisberg & Kalluri, 2013) and also as critical elements in the stroma reaction to epithelial tumors (Otranto et al., 2012). To date, no effective antifibrotic therapies are available (Miao et al., 2021; Sassoli, Nistri, et al., 2022). In this scenario a deeper understanding of fibroblast-to-Myof transition and of Myofs' biology appears fundamental for aiding in the identification of novel potential therapeutic targets.

This study showed that HT can represent a valid approach to morphologically distinguish fibroblasts from well differentiated Myofs.

Indeed, HT imaging unraveled the morphological features typical of a Myof. Among them, HT uncovered an increased polygonal shape, a more elongated nucleus, the presence of filamentous structures across the cytoplasm, clustered structures at the membrane periphery and a network of cytoplasmic membranous structures surrounding the nucleus. In particular, the filamentous structures are referable to actin containing stress fibers and the clustered structures may likely correspond to focal adhesion plaques. On the other hand, the network of membranous structures can represent membrane-bound organelles such as mitochondria and cell synthesizing apparatus (endoplasmic reticulum and Golgi apparatus).

Notably, such morphological details acquired by HT were perfectly accordant with the morphological features unraveled by CLS microscopy analyses. Indeed CLS microscopy observations confirmed in the more differentiated cells the formation of robust F-actin structures containing α -sma and p-MLC2, the presence of vinculin-enriched focal adhesion plaques, numerous mitochondria associated with an increased expression of PGC-1 α and an augment of Col-I expression indicative of a cell in an active phase of ECM synthesis.

The major advantage of HT relies on its ability to identify the peculiar features of living cells by exploiting the intrinsic optical properties of the cells (RI) that cannot be achieved by the conventional optical microscopy without using any kind of labeling. Therefore, HT does not require time-consuming sample preparation and it does not alter or damage the biological sample during imaging. The 3D RI tomograms are not susceptible to ungovernable alterations such as the photobleaching. Moreover, HT uses a very low-power light source thus avoiding phototoxic effects. Noteworthy, HT RI maps-based quantitative analysis provided objective measures concerning biophysical and biochemical parameters, corroborating the morphological observations and strengthening the results. Indeed volume, surface area and projection area of the individual whole cell induced to differentiate by treatment with TGF- β 1, increased as compared to proliferating fibroblasts and during the differentiation time. In particular, the increase in cell surface is also supported by the electrophysiological evaluation of membrane capacitance (Cm), which showed a parallel increase with the differentiation time. At the same time, we found that the sphericity index slightly decreased. Sphericity index is a dimensionless parameter that quantifies the degree of cell roundness, thus providing indications on the shape of the cell on the degree of flattening or grade of adhesion of the cell to the substrate. All these data reflect the progressive enlargement of the cells undergoing transition towards Myofs, their polygonal shaping and likely adhesion to the substrate due to the actin filament polymerization and assembly progression. Moreover, the change in cell sphericity may be associated with the contractile function of differentiated Myofs necessary *in vivo* to exert traction forces on the tissue, the wound closure or contracture in the scar tissue (Hinze et al., 2019; Pakshir et al., 2020). Again, such data aligned with CSL analyses of F-actin and p-MLC2 expression.

Of interest, all these morphological data highlighting the features of fibroblasts and Myofs, were substantiated by the functional electrophysiological analyses that confirmed the acquisition of a more

mature cell phenotype by the cells culture in DM. Apart from the membrane capacitance values, which can be directly related to morphological features, we observed a RMP depolarization in the differentiated cells, which can facilitate Myof contractile activity, and an increase in the TRPC1 currents which is in line with the acquisition of a more functional phenotype (Sassoli et al., 2016). Furthermore, we may also suppose a correlation between the rise of TRPC1 channels' functionality and the stress fiber assembly observed in differentiated cells. Indeed, TRPC1 channel, besides acting as a store-operated Ca^{2+} entry channel (SOC), has been demonstrated to represent an essential component of stretch-activated channels (SACs) in different cell types including fibroblasts and Myofs and to be an integral part of the adhesion plaque linked to cytoskeleton (Formigli et al., 2009; Li et al., 2024; Sassoli et al., 2016). In such a view TRPC1 opening may be modulated by the action of cytoskeletal remodeling and stress fiber formation capable to transmit forces to plasmamembrane (Formigli et al., 2007; Sbrana et al., 2008).

As far the mean dry mass values of the whole cell is concerned, we found that it significantly increased over the differentiation time with respect to the proliferation condition, reaching the maximum values at the time when the cell exhibits a well differentiated Myof phenotype. The dry mass is the amount of non-aqueous constituents of the cell such as carbohydrates, proteins, lipids and nucleic acids and represents a valid indicator of the anabolic and catabolic processes occurring within a cell. These data are in good agreement with the maturation of the focal adhesion and the stress-fiber formation as well as the increase of the ECM synthesizing activity of the differentiated cells. These events occurring during fibroblast-to-Myof differentiation were confirmed here and documented in the literature (Cappitti et al., 2023; Chellini, Tani, Vallone, Nosi, Pavan, Bambi, & Sassoli, 2018; Noom et al., 2024; Pakshir et al., 2020; Sassoli et al., 2013; Sassoli et al., 2016; Sassoli, Garella, et al., 2022; Squecco et al., 2015; Younesi et al., 2024). Moreover, quantification of volume, surface area, projection area and sphericity index of nuclei unraveled that the nuclei increased their size and acquired a more elongated shape in the differentiating cells as compared to not differentiating ones. Given the existence of a connection between cytoskeleton and the nucleoskeleton through transmembrane complexes in the nuclear envelope (Stancheva & Schirmer, 2014), the present results may be dependent by the action of mechanical forces generated by contractile stress fibers on the nucleus able to deform it. In turn, this may impact chromatin organization/remodeling and regulate gene expression (Adam, 2017; Miroshnikova & Wickström, 2022). By contrast, the mean values of the dry mass of the nuclei were comparable between proliferating and differentiating cells. This observation might be in line with previous studies showing the stability of the nuclear compartment against perturbation (Kim & Guck, 2020). As far as the quantitative analysis of the volume and the dry mass of the nucleoli is concerned, it did not reveal a significant difference in such values among all the different experimental conditions. Of note, HT images reveal a different number of nucleoli in proliferating and differentiating cells. In particular more differentiated cells exhibited a minor number of such sub-nuclear structures as observed for other cell types undergoing differentiation (Flick Jaecker et al., 2022; Miyake &

McDermott, 2023; Pitolitsyna et al., 2024; Rodrigues et al., 2023; Smetana et al., 2020). The changes in the organization of nucleoli that primarily function as a factory for rRNA transcription and ribosome biogenesis (Goodfellow & Zomerdiik, 2013) might be correlable to the changes in the protein translational capacity of the cells.

5 | CONCLUSION

Our study reveals the remarkable imaging capacity of HT to distinguish proliferating fibroblasts from differentiated Myofs in a non-invasive and rapid way without the use of specific labeling, quantitatively discriminating cell properties according to RI. We envision that this imaging approach can improve our understanding of fibroblast-to-Myof transition and Myofs' biology and contribute to unlocking new research opportunities in the field of fibrosis. The main limitation of the present method is the lack of molecular specificity that, however, can be overcome by combining HT with other imaging, biochemical and biomolecular approaches. We emphasize that the HT imaging technique exploited here is not limited to the cells targeted in this study and that it may represent an advantage and an attractive tool for studying for example delicate cells that could be affected by traditional staining methods.

AUTHOR CONTRIBUTIONS

Francesca Sbrana: Conceptualization; methodology; validation; investigation; resources; data curation; writing – original draft; writing – review and editing; visualization; formal analysis; funding acquisition. **Flaminia Chellini:** Methodology; validation; investigation; resources; data curation; writing – review and editing; formal analysis; funding acquisition. **Alessia Tani:** Methodology; investigation; validation; data curation; writing – review and editing. **Martina Parigi:** Investigation; writing – review and editing. **Rachele Garella:** Investigation; validation; writing – review and editing. **Francesco Palmieri:** Investigation; validation; data curation; formal analysis; writing – review and editing. **Sandra Zecchi-Orlandini:** Writing – review and editing; resources. **Roberta Squecco:** Methodology; investigation; resources; validation; data curation; writing – original draft; writing – review and editing; formal analysis; visualization; funding acquisition. **Chiara Sassoli:** Conceptualization; methodology; resources; validation; data curation; writing – original draft; writing – review and editing; visualization; supervision; project administration; funding acquisition; investigation.

ACKNOWLEDGMENTS

The authors would like to thank Dr. Debora Burini for her skillful technical assistance. Particular thanks to Schaefer South-East Europe Srl for granting us the opportunity to perform analysis by means of HT microscope.

FUNDING INFORMATION

This research was funded by MUR (Ministry of University and Research, Italy) – Finanziamenti alla Ricerca di Ateneo ex 60% – University of Florence to Flaminia Chellini, Sandra Zecchi-Orlandini, Roberta Squecco and Chiara Sassoli and partially by the European

Commission, NextGenerationEU, Missione 4 Componente 2, "Dalla ricerca all'impresa", Innovation Ecosystem RAISE "Robotics and AI for Socio-economic Empowerment", ECS00000035 to Francesca Sbrana.

CONFLICT OF INTEREST STATEMENT

The authors declare no conflicts of interest.

DATA AVAILABILITY STATEMENT

The data that support the findings of this study are available from the corresponding author upon reasonable request.

ORCID

Chiara Sassoli  <https://orcid.org/0000-0002-1337-0938>

REFERENCES

- Adam, S. A. (2017). The nucleoskeleton. *Cold Spring Harbor Perspectives in Biology*, 9(2), a023556. <https://doi.org/10.1101/cshperspect.a023556>
- Barer, R. (1953). Determination of dry mass, thickness, solid and water concentration in living cells. *Nature*, 172(4389), 1097–1098. <https://doi.org/10.1038/1721097a0>
- Cappitti, A., Palmieri, F., Garella, R., Tani, A., Chellini, F., Salzano De Luna, M., Parmeggiani, C., Squecco, R., Martella, D., & Sassoli, C. (2023). Development of accessible platforms to promote myofibroblast differentiation by playing on hydrogel scaffold composition. *Biomaterials Advances*, 155, 213674. <https://doi.org/10.1016/j.bioadv.2023.213674>
- Chellini, F., Tani, A., Vallone, L., Nosi, D., Pavan, P., Bambi, F., & Sassoli, C. (2018). Platelet-rich plasma prevents in vitro transforming growth factor- β 1-induced fibroblast to myofibroblast transition: Involvement of vascular endothelial growth factor (VEGF)-A/VEGF receptor-1-mediated signaling. *Cells*, 7(9), 142. <https://doi.org/10.3390/cells7090142>
- Chellini, F., Tani, A., Vallone, L., Nosi, D., Pavan, P., Bambi, F., Zecchi-Orlandini, S., & Sassoli, C. (2018). Platelet-rich plasma and bone marrow-derived mesenchymal stromal cells prevent TGF- β 1-induced myofibroblast generation but are not synergistic when combined: Morphological in vitro analysis. *Cells, Tissues, Organs*, 206(6), 283–295. <https://doi.org/10.1159/000501499>
- Chilton, L., Ohya, S., Freed, D., George, E., Drobnic, V., Shibukawa, Y., Maccannell, K. A., Imaizumi, Y., Clark, R. B., Dixon, I. M. C., & Giles, W. R. (2005). K⁺ currents regulate the resting membrane potential, proliferation, and contractile responses in ventricular fibroblasts and myofibroblasts. *American Journal of Physiology. Heart and Circulatory Physiology*, 288, 2931–2939. <https://doi.org/10.1152/ajpheart.01220.2004>
- Choi, S. Y., Oh, J., Jung, J., Park, Y., & Lee, S. Y. (2021). Three-dimensional label-free visualization and quantification of polyhydroxyalkanoates in individual bacterial cell in its native state. *Proceedings of the National Academy of Sciences of the United States of America*, 118(31), e2103956118. <https://doi.org/10.1073/pnas.2103956118>
- Combe, C. L., Upchurch, C. M., Canavier, C. C., & Gasparini, S. (2023). Cholinergic modulation shifts the response of CA1 pyramidal cells to depolarizing ramps via TRPM4 channels with potential implications for place field firing. *eLife*, 12, e84387. <https://doi.org/10.7554/eLife.84387>
- Costa, E., Gambardella, C., Miroglio, R., Di Giannantonio, M., Lavorano, S., Minetti, R., Sbrana, F., Piazza, V., Faimali, M., & Garaventa, F. (2023). Nanoplastic uptake temporarily affects the pulsing behavior in ephyrae of the moon jellyfish *Aurelia* sp. *Ecotoxicology*, 32, 618–627. <https://doi.org/10.1007/s10646-023-02669-0>
- Devaney, A. J. (1981). Inverse-scattering theory within the Rytov approximation. *Optics Letters*, 6(8), 374–376. <https://doi.org/10.1364/OL.6.000374>
- Di Giannantonio, M., Gambardella, C., Miroglio, R., Costa, E., Sbrana, F., Smerieri, M., Carraro, G., Utzeri, R., Faimali, M., & Garaventa, F. (2022). Ecotoxicity of polyvinylidene difluoride (PVDF) and polylactic acid (PLA) microplastics in marine zooplankton. *Toxics*, 10, 479. <https://doi.org/10.3390/toxics10080479>
- Flick Jaecker, F., Almeida, J. A., Krull, C. M., & Pathak, A. (2022). Nucleoli in epithelial cell collectives respond to tumorigenic, spatial, and mechanical cues. *Molecular Biology of the Cell*, 33(11), br19. <https://doi.org/10.1091/mbc.E22-02-0070>
- Formigli, L., Meacci, E., Sassoli, C., Squecco, R., Nosi, D., Chellini, F., Naro, F., Francini, F., & Zecchi-Orlandini, S. (2007). Cytoskeleton/stretch-activated ion channel interaction regulates myogenic differentiation of skeletal myoblasts. *Journal of Cellular Physiology*, 211(2), 296–306. <https://doi.org/10.1002/jcp.20936>
- Formigli, L., Sassoli, C., Squecco, R., Bini, F., Martinesi, M., Chellini, F., Luciani, G., Sbrana, F., Zecchi-Orlandini, S., Francini, F., & Meacci, E. (2009). Regulation of transient receptor potential canonical channel 1 (TRPC1) by sphingosine 1-phosphate in C2C12 myoblasts and its relevance for a role of mechanotransduction in skeletal muscle differentiation. *Journal of Cell Science*, 122(Pt 9), 1322–1333. <https://doi.org/10.1242/jcs.035402>
- Friedrich, R. P., Schreiber, E., Tietze, R., Yang, H., Pilarsky, C., & Alexiou, C. (2020). Intracellular quantification and localization of label-free iron oxide nanoparticles by holotomographic microscopy. *Nanotechnology, Science and Applications*, 13, 119–130. <https://doi.org/10.2147/NSA.S282204>
- Goodfellow, S. J., & Zomerdijk, J. C. (2013). Basic mechanisms in RNA polymerase I transcription of the ribosomal RNA genes. *Sub-Cellular Biochemistry*, 61, 211–236. https://doi.org/10.1007/978-94-007-4525-4_10
- Hinz, B., McCulloch, C. A., & Coelho, N. M. (2019). Mechanical regulation of myofibroblast phenocconversion and collagen contraction. *Experimental Cell Research*, 379(1), 119–128. <https://doi.org/10.1016/j.yexcr.2019.03.027>
- Hugonnet, H., Kim, Y. W., Lee, M., Shin, S., Hruban, R. H., Hong, S.-M., & Park, Y. (2021). Multiscale label-free volumetric holographic histopathology of thick-tissue slides with subcellular resolution. *Advanced Photonics*, 3, 026004-1. <https://doi.org/10.1117/1.AP.3.2.026004>
- Jung, J., Hong, S.-J., Kim, H.-B., Kim, G., Lee, M., Shin, S., Lee, S., Kim, D.-J., Lee, C.-G., & Park, Y. (2018). Label-free non-invasive quantitative measurement of lipid contents in individual microalgal cells using refractive index tomography. *Scientific Reports*, 8(1), 6524. <https://doi.org/10.1038/s41598-018-24393-0>
- Kang, S. H., Shin, Y. S., Lee, D.-H., Park, S., Kim, S. K., Ryu, D., Park, Y., Byun, S.-H., Choi, J.-H., & Hong, S. J. (2022). Interactions of nanoparticles with macrophages and feasibility of drug delivery for asthma. *International Journal of Molecular Sciences*, 23(3), 1622. <https://doi.org/10.3390/ijms23031622>
- Kaur, K., Zarzoso, M., Ponce-Balbuena, D., Guerrero-Serna, G., Hou, L., Musa, H., & Jalife, J. (2013). TGF- β 1, released by myofibroblasts, differentially regulates transcription and function of sodium and potassium channels in adult rat ventricular myocytes. *PLoS One*, 8, e55391. <https://doi.org/10.1371/journal.pone.0055391>
- Kim, G., Jo, Y., Cho, H., Min, H.-S., & Park, Y. (2019). Learning-based screening of hematologic disorders using quantitative phase imaging of individual red blood cells. *Biosensors & Bioelectronics*, 123, 69–76. <https://doi.org/10.1016/j.bios.2018.09.068>
- Kim, G., Lee, S., Shin, S., & Park, Y. (2018). Three-dimensional label-free imaging and analysis of Pinus pollen grains using optical diffraction tomography. *Scientific Reports*, 8(1), 1782. <https://doi.org/10.1038/s41598-018-20113-w>
- Kim, K., & Guck, J. (2020). The relative densities of cytoplasm and nuclear compartments are robust against strong perturbation. *Biophysical Journal*, 119(10), 1946–1957. <https://doi.org/10.1016/j.bpj.2020.08.044>
- Kim, K., Kim, K. S., Park, H., Ye, J. C., & Park, Y. (2013). Real-time visualization of 3-D dynamic microscopic objects using optical diffraction tomography. *Optics Express*, 21(26), 32269–32278. <https://doi.org/10.1364/OE.21.032269>
- Kim, K., Lee, S., Yoon, J., Heo, J., Choi, C., & Park, Y. (2016). Three-dimensional label-free imaging and quantification of lipid droplets in live

- hepatocytes. *Scientific Reports*, 6, 36815. <https://doi.org/10.1038/srep36815>
- Kim, K., Yoon, H., Diez-Silva, M., Dao, M., Dasari, R. R., & Park, Y. (2014). High-resolution three-dimensional imaging of red blood cells parasitized by *Plasmodium falciparum* and in situ hemozoin crystals using optical diffraction tomography. *Journal of Biomedical Optics*, 19(1), 011005. <https://doi.org/10.1117/1.JBO.19.1.011005>
- Kim, K., Yoon, J., Shin, S., Lee, S. Y., Yang, S.-A., & Park, Y. (2016). Optical diffraction tomography techniques for the study of cell pathophysiology. *Journal of Biomedical Photonics & Engineering*, 2(2), 020201. <https://doi.org/10.18287/JBPE.16.02.020201>
- Kim, S.-Y., Lee, J.-H., Shin, Y., Kim, T.-K., Lee, J. W., Pyo, M. J., Lee, A. R., Pack, C.-G., & Cho, Y. S. (2022). Label-free imaging and evaluation of characteristic properties of asthma-derived eosinophils using optical diffraction tomography. *Biochemical and Biophysical Research Communications*, 587, 42–48. <https://doi.org/10.1016/j.bbrc.2021.11.084>
- Kim, Y. S., Lee, S., Jung, J., Shin, S., Choi, H.-G., Cha, G.-H., Park, W., Lee, S., & Park, J. (2018). Combining three-dimensional quantitative phase imaging and fluorescence microscopy for the study of cell pathophysiology. *The Yale Journal of Biology and Medicine*, 91(3), 267–277.
- Koo, S. E., Jang, S., Park, Y., & Park, C. J. (2019). Reconstructed three-dimensional images and parameters of individual erythrocytes using optical diffraction tomography microscopy. *Annals of Laboratory Medicine*, 39, 223–226. <https://doi.org/10.3343/alm.2019.39.2.223>
- Lee, A. J., Hugonnet, H., Kim, Y. S., Kim, J.-G., Lee, M., Ku, T., & Park, Y. (2023). Volumetric refractive index measurement and quantitative density analysis of mouse brain tissue with sub-micrometer spatial resolution. *Advanced Photonics Research*, 4, 202300112. <https://doi.org/10.1002/adpr.202300112>
- Lee, M., Lee, Y.-H., Song, J., Kim, G., Jo, Y., Min, H., Kim, C. H., & Park, Y. (2020). Deep-learning-based three-dimensional label-free tracking and analysis of immunological synapses of CAR-T cells. *eLife*, 9, e49023. <https://doi.org/10.7554/eLife.49023>
- Li, S., Qu, L., Zhou, L., Zhan, N., Liu, L., Ling, Y., Chen, Q., Lai, W., Lin, N., & Li, J. (2024). Biomass fuels related-PM2.5 promotes lung fibroblast-myofibroblast transition through PI3K/AKT/TRPC1 pathway. *Ecotoxicology and Environmental Safety*, 276, 116309. <https://doi.org/10.1016/j.ecoenv.2024.116309>
- Mannelli, M., Gamberi, T., Garella, R., Magherini, F., Squecco, R., & Fiaschi, T. (2022). Pyruvate prevents the onset of the cachectic features and metabolic alterations in myotubes downregulating STAT3 signaling. *The FASEB Journal*, 36(11), e22598. <https://doi.org/10.1096/fj.202200848R>
- Martella, D., Mannelli, M., Squecco, R., Garella, R., Idrizaj, E., Antonioli, D., Laus, M., Wiersma, D. S., Gamberi, T., Paoli, P., Parmeggiani, C., & Fiaschi, T. (2021). Cell instructive liquid crystalline networks for myotube formation. *iScience*, 24(9), 103077. <https://doi.org/10.1016/j.isci.2021.103077>
- Miao, H., Wu, X.-Q., Zhang, D.-D., Wang, Y.-N., Guo, Y., Li, P., & Zhao, Y.-Y. (2021). Deciphering the cellular mechanisms underlying fibrosis-associated diseases and therapeutic venues. *Pharmacological Research*, 163, 105316. <https://doi.org/10.1016/j.phrs.2020.105316>
- Miroshnikova, Y. A., & Wickström, S. A. (2022). Mechanical forces in nuclear organization. *Cold Spring Harbor Perspectives in Biology*, 14(1), a039685. <https://doi.org/10.1101/cshperspect.a039685>
- Miyake, T., & McDermott, J. C. (2023). Re-organization of nucleolar architecture in myogenic differentiation. *Journal of Cell Science*, 136(4), jcs260496. <https://doi.org/10.1242/jcs.260496>
- Negmadjanov, U., Godic, Z., Rizvi, F., Emelyanova, L., Ross, G., Richards, J., Holmuhamedov, E. L., & Jahangir, A. (2015). TGF- β 1-Mediated differentiation of fibroblasts is associated with increased mitochondrial content and cellular respiration. *PLoS One*, 10(4), e0123046. <https://doi.org/10.1371/journal.pone.0123046>
- Noom, A., Sawitzki, B., Knaus, P., & Duda, G. N. (2024). A two-way street – cellular metabolism and myofibroblast contraction. *npj Regenerative Medicine*, 9(1), 15. <https://doi.org/10.1038/s41536-024-00359-x>
- Oh, J., Ryu, J. S., Lee, M., Jung, J., Han, S., Chung, H. J., & Park, Y. (2020). Three-dimensional label-free observation of individual bacteria upon antibiotic treatment using optical diffraction tomography. *Biomedical Optics Express*, 11(3), 1257–1267. <https://doi.org/10.1364/BOE.377740>
- Otranto, M., Sarrazy, V., Bonté, F., Hinz, B., Gabbiani, G., & Desmoulière, A. (2012). The role of the myofibroblast in tumor stroma remodeling. *Cell Adhesion & Migration*, 6, 203–219. <https://doi.org/10.4161/cam.20377>
- Pakshir, P., Noskovicova, N., Lodyga, M., Son, D. O., Schuster, R., Goodwin, A., Karvonen, H., & Hinz, B. (2020). The myofibroblast at a glance. *Journal of Cell Science*, 133(13), jcs227900. <https://doi.org/10.1242/jcs.227900>
- Park, H., Lee, S., Ji, M., Kim, K., Son, Y., Jang, S., & Park, Y. (2016). Measuring cell surface area and deformability of individual human red blood cells over blood storage using quantitative phase imaging. *Scientific Reports*, 6, 34257. <https://doi.org/10.1038/srep34257>
- Park, Y., Depeursinge, C., & Popescu, G. (2018). Quantitative phase imaging in biomedicine. *Nature Photonics*, 12, 578–589. <https://doi.org/10.1038/s41566-018-0253-x>
- Popescu, G., Park, Y., Lue, N., Best-Popescu, C., Deflores, L., Dasari, R. R., Feld, M. S., & Badizadegan, K. (2008). Optical imaging of cell mass and growth dynamics. *American Journal of Physiology. Cell Physiology*, 295, C538–C544. <https://doi.org/10.1152/ajpcell.00121.2008>
- Potolitsyna, E., Pickering, S. H., Bellanger, A., Germier, T., Collas, P., & Briand, N. (2024). Cytoskeletal rearrangement precedes nucleolar remodeling during adipogenesis. *Communications Biology*, 7(1), 458. <https://doi.org/10.1038/s42003-024-06153-1>
- Rodrigues, A., MacQuarrie, K. L., Freeman, E., Lin, A., Willis, A. B., Xu, Z., Alvarez, A. A., Ma, Y., White, B. E. P., Foltz, D. R., & Huang, S. (2023). Nucleoli and the nucleoli-centromere association are dynamic during normal development and in cancer. *Molecular Biology of the Cell*, 34(4), br5. <https://doi.org/10.1091/mbc.E22-06-0237>
- Ryu, D., Bak, T., Ahn, D., Kang, H., Oh, S., Min, H. S., Lee, S., & Lee, J. (2023). Deep learning-based label-free hematology analysis framework using optical diffraction tomography. *Heliyon*, 9(8), e18297. <https://doi.org/10.1016/j.heliyon.2023.e18297>
- Salucci, S., Battistelli, M., Burattini, S., Sbrana, F., & Falcieri, E. (2020). Holotomographic microscopy: A new approach to detect apoptotic cell features. *Microscopy Research and Technique*, 83(12), 1464–1470. <https://doi.org/10.1002/jemt.23539>
- Sassoli, C. (2022). Fibrosis: From cellular and molecular targets to therapeutic strategies. *Current Molecular Medicine*, 22(3), 193–195. <https://doi.org/10.2174/156652402203220314140908>
- Sassoli, C., Chellini, F., Pini, A., Tani, A., Nistri, S., Nosi, D., Zecchi-Orlandini, S., Bani, D., & Formigli, L. (2013). Relaxin prevents cardiac fibroblast-myofibroblast transition via notch-1-mediated inhibition of TGF- β /Smad3 signaling. *PLoS One*, 8(5), e63896. <https://doi.org/10.1371/journal.pone.0063896>
- Sassoli, C., Chellini, F., Squecco, R., Tani, A., Idrizaj, E., Nosi, D., Giannelli, M., & Zecchi-Orlandini, S. (2016). Low intensity 635 nm diode laser irradiation inhibits fibroblast-myofibroblast transition reducing TRPC1 channel expression/activity: New perspectives for tissue fibrosis treatment. *Lasers in Surgery and Medicine*, 48(3), 318–332. <https://doi.org/10.1002/lsm.22441>
- Sassoli, C., Garella, R., Chellini, F., Tani, A., Pavan, P., Bambi, F., Zecchi-Orlandini, S., & Squecco, R. (2022). Platelet-rich plasma affects gap junctional features in myofibroblasts in vitro via vascular endothelial growth factor (VEGF)-A/VEGF receptor. *Experimental Physiology*, 107(2), 106–121. <https://doi.org/10.1113/EP090052>
- Sassoli, C., Nistri, S., Chellini, F., & Bani, D. (2022). Human recombinant relaxin (serelaxin) as anti-fibrotic agent: Pharmacology, limitations and actual perspectives. *Current Molecular Medicine*, 22(3), 196–208. <https://doi.org/10.2174/1566524021666210309113650>
- Sbrana, F., Sassoli, C., Meacci, E., Nosi, D., Squecco, R., Paternostro, F., Tiribilli, B., Zecchi-Orlandini, S., Francini, F., & Formigli, L. (2008). Role

- for stress fiber contraction in surface tension development and stretch-activated channel regulation in C2C12 myoblasts. *American Journal of Physiology. Cell Physiology*, 295(1), C160–C172. <https://doi.org/10.1152/ajpcell.00014.2008>
- Smetana, K., Klamová, H., & Mikulenková, D. (2020). Dominant nucleolus in the progenitor cell using human bone marrow erythroid and granulocytic cell lineages as a model. A morphological and cytochemical note. *Folia Biologica (Praha)*, 66(3), 111–115.
- Squecco, R., Chellini, F., Idrizaj, E., Tani, A., Garella, R., Pancani, S., & Sassoli, C. (2020). Platelet-rich plasma modulates gap junction functionality and connexin 43 and 26 expression during TGF- β 1-induced fibroblast to myofibroblast transition: Clues for counteracting fibrosis. *Cells*, 9(5), 1199. <https://doi.org/10.3390/cells9051199>
- Squecco, R., Luciani, P., Idrizaj, E., Deledda, C., Benvenuti, S., Giuliani, C., Fibbi, B., Peri, A., & Francini, F. (2016). Hyponatraemia alters the biophysical properties of neuronal cells independently of osmolarity: A study on Ni(2+) -sensitive current involvement. *Experimental Physiology*, 101(8), 1086–1100. <https://doi.org/10.1113/EP085806>
- Squecco, R., Sassoli, C., Garella, R., Chellini, F., Idrizaj, E., Nistri, S., Formigli, L., Bani, D., & Francini, F. (2015). Inhibitory effects of relaxin on cardiac fibroblast-to-myofibroblast transition: An electrophysiological study. *Experimental Physiology*, 100, 652–666. <https://doi.org/10.1113/EP085178>
- Stancheva, I., & Schirmer, E. C. (2014). Nuclear envelope: Connecting structural genome organization to regulation of gene expression. *Advances in Experimental Medicine and Biology*, 773, 209–244. https://doi.org/10.1007/978-1-4899-8032-8_10
- Tomasek, J. J., Gabbiani, G., Hinz, B., Chaponnier, C., & Brown, R. A. (2002). Myofibroblasts and mechano-regulation of connective tissue remodelling. *Nature Reviews. Molecular Cell Biology*, 3(5), 349–363. <https://doi.org/10.1038/nrm809>
- Weiskirchen, R., Weiskirchen, S., & Tacke, F. (2019). Organ and tissue fibrosis: Molecular signals, cellular mechanisms and translational implications. *Molecular Aspects of Medicine*, 65, 2–15. <https://doi.org/10.1016/j.mam.2018.06.003>
- Wolf, E. (1969). Three-dimensional structure determination of semi-transparent objects from holographic data. *Optics Communication*, 1(4), 153–156. [https://doi.org/10.1016/0030-4018\(69\)90052-2](https://doi.org/10.1016/0030-4018(69)90052-2)
- Yang, S.-A., Yoon, J., Kim, K., & Park, Y. (2017). Measurements of morphological and biochemical alterations in individual neuron cells associated with early neurotoxic effects in Parkinson's disease using optical diffraction tomography. *Cytometry, Part A*, 91(5), 510–518. <https://doi.org/10.1002/cyto.a.23110>
- Yoon, J., Jo, Y., Kim, M.-H., Kim, K., Lee, S., Kang, S.-J., & Park, Y. (2017). Identification of non-activated lymphocytes using three-dimensional refractive index tomography and machine learning. *Scientific Reports*, 7(1), 6654. <https://doi.org/10.1038/s41598-017-06311-y>
- Younesi, F. S., Miller, A. E., Barker, T. H., Rossi, F. M. V., & Hinz, B. (2024). Fibroblast and myofibroblast activation in normal tissue repair and fibrosis. *Nature Reviews. Molecular Cell Biology*. <https://doi.org/10.1038/s41580-024-00716-0> Online ahead of print.
- Zangle, T. A., & Teitell, M. A. (2014). Live-cell mass profiling: An emerging approach in quantitative biophysics. *Nature Methods*, 11(12), 1221–1228. <https://doi.org/10.1038/nmeth.3175>
- Zeisberg, M., & Kalluri, R. (2013). Cellular mechanisms of tissue fibrosis. 1. Common and organ-specific mechanisms associated with tissue fibrosis. *American Journal of Physiology-Cell Physiology*, 304(3), C216–C225. <https://doi.org/10.1152/ajpcell.00328.2012>
- Zhao, H., Brown, P. H., & Schuck, P. (2011). On the distribution of protein refractive index increments. *Biophysical Journal*, 100(9), 2309–2317. <https://doi.org/10.1016/j.bpj.2011.03.004>

SUPPORTING INFORMATION

Additional supporting information can be found online in the Supporting Information section at the end of this article.

How to cite this article: Sbrana, F., Chellini, F., Tani, A., Parigi, M., Garella, R., Palmieri, F., Zecchi-Orlandini, S., Squecco, R., & Sassoli, C. (2024). Label-free three-dimensional imaging and quantitative analysis of living fibroblasts and myofibroblasts by holotomographic microscopy. *Microscopy Research and Technique*, 1–17. <https://doi.org/10.1002/jemt.24648>